

Date of publication xxxx 00, 0000, date of current version xxxx 00, 0000.

Digital Object Identifier 10.1109/ACCESS.2017.DOI

Position and Cross-Coupling Factors Estimation for Sliding Mode Current Control based Position-Sensorless Control of IPMSM

KEITA SHIMAMOTO^{1,2}, (Member, IEEE)
AND TOSHIYUKI MURAKAMI³, (Senior Member, IEEE)

¹Tsukuba Research Laboratory, YASKAWA Electric Corporation, Tsukuba, 300-2635, Japan (e-mail: Keita.Shimamoto@yaskawa.co.jp)

²Graduate School of Science and Technology, Keio University, Yokohama, 223-8522, Japan

³Department of System Design Engineering, Keio University, Yokohama, 223-8522, Japan (e-mail: mura@sd.keio.ac.jp)

Corresponding author: Keita Shimamoto (e-mail: Keita.Shimamoto@yaskawa.co.jp).

ABSTRACT This paper presents a control method with an estimation method of cross-coupling factors of Interior Permanent Magnet Synchronous Motors (IPMSM) inductance for position-sensorless servo drive systems. The cross-coupling factors are from dq-axis mutual inductance. Conventionally, the cross-coupling factors have been ignored in the IPMSM model and deteriorate control performance. That has caused decreasing robustness and velocity vibration in the low-speed range. Since the cross-coupling factors vary with the rotor position and the current, it is hard to measure them. Therefore, the proposed method utilizes a high-frequency voltage injection method to estimate the cross-coupling factors online. In addition, the proposed current control method utilizes a sliding mode control and voltage disturbance observer based on the voltage equation, including the dq-axis mutual inductance model. The estimated cross-coupling factors are reflected in the proposed current controller instantaneously. Experimental results show that the proposed method considering cross-coupling factors increases the robustness to the disturbance force and reduces the velocity vibration.

INDEX TERMS Current control, dq-axis mutual inductance, Parameter estimation, Sliding mode control, Voltage disturbance observer

I. INTRODUCTION

RECENTLY, Interior Permanent Magnet Synchronous Motors (IPMSMs) have been widely utilized in industrial applications as servo drive systems. The demand for servo drive systems for automation and cooperative operation between machines and workers is growing in many fields, not limited to factories. Significantly, the expectations have been rising for machines to be used outdoors. To realize the system for using outdoors, much higher torque density and higher robustness to dust, water, and temperature are required for the servo drive systems with IPMSMs. One of the methods to respond to the requirements is a position-sensorless servo drive system [1], [2].

Position sensors such as encoders have been attached to the IPMSMs to detect the rotor position for efficient and precise operation. Position sensors are precision equipment and

unsuitable in harsh environments such as dusty, high temperature, or vibrated environments. IPMSMs without encoders are applicable in those harsh environments. In addition, by removing these sensors, the motor size and weight can be decreased, as shown in Fig. 1. As a result, the torque density of the system can be higher. According to these advantages, the position-sensorless control methods and position estimation methods have also been attracted more attention.

Various position estimation methods have been proposed. In medium-speed or high-speed operation, position estimation methods that utilize back-electromotive force (EMF) have been widely used [3], [4], [5]. However, back-EMF is hard to be detected at low-speed, including zero-speed. In applications of servo drive systems, low-speed operation and positioning are essential. In these operations, magnetic saliency-based estimation methods are appropriate since



FIGURE 1. Comparison of position-sensorless servomotor.

these methods utilize high-frequency voltage or current [6], [7], [8], [9].

Magnetic saliency-based position estimation methods utilize high-frequency voltage or current. Some methods with square-wave-type voltage synchronized carrier frequency have been proposed to minimize the delay in the estimation processing and realize a higher response of position estimation [10]. However, this estimation processing is based on a voltage equation without considering dq-axis mutual inductance, which is varied depending on the position and the load current. [11], [12], [13]. Since the dq-axis mutual inductance terms are not expressed in the general dq-axis voltage equation, which is derived by the geometric transformation between UVW-phase and dq-phase, the inductance has been ignored. The models that ignore the dq-axis mutual inductance cause errors of the estimated position. However, in actual use, local magnetic saturation may increase or decrease in the motor core, and the q-axis magnetic flux crosses the coil on the d-axis side or vice versa. In addition, the passes of the magnetic flux are biased and varied depending on the position due to spatial harmonic components such as slot harmonics [14]. References [12], [13], and [15] give examples to decrease the position estimation error by considering dq-axis mutual inductance with parameters obtained by previous analyses such as finite element analysis (FEA). The reference [12] focused on the dq-axis mutual inductance varied with the load current. On the other hand, the reference [13] focused on not only the load current but also the spatial harmonic components. The reference [16] revealed that dq-axis mutual inductance affects current control and ripples. Although these methods showed that considering dq-axis mutual inductance increases the performance of current control and position estimation, they require previous analyses.

A position and dq-axis mutual inductance estimation method without previous analyses have been proposed [17], [18]. These results showed the position estimation performance increase and high-frequency velocity vibration reduction. In addition, a current control method considering dq-axis mutual inductance that was estimated online has been proposed [19]. The high-frequency velocity vibration was smaller than that without considering dq-axis mutual inductance. However, further performance evaluation was required. Further improvement of the current control to derive the voltage command and evaluation of the estimation accuracy are expected to reduce the vibration more.

Generally, voltage commands are required to apply ap-

propriate voltage to motors with voltage source inverter devices. The voltage command is calculated by field-oriented control (FOC) with proportional-integral controller (PI) or direct torque control (DTC) for position-sensorless control. Though improved DTC methods for low-speed operations have been proposed, the performance of these methods is sensitive to inductance parameters [20], [21]. As shown in [16], inductance parameters are dynamically changed during operation. FOC with high PI gains can compensate for disturbances such as modeling errors or parameter variations. However, the PI gains of position-sensorless servo drive systems cannot be as high as those of servo drive systems with position sensors. One of the robust control methods that can deal with uncertainty is sliding mode control (SMC). SMC has often been used as sliding mode observers for position estimation to avoid the performance deterioration from electrical disturbance [22], [23]. Conventional models for sliding mode observers utilize general voltage equations without considering dq-axis mutual inductance.

This paper presents SMC and voltage disturbance observer (VDOB) considering dq-axis mutual inductance for position-sensorless servo drive systems. This paper also reveals that the estimated dq-axis mutual inductance values have been part of the actual values in discrete-time systems. Therefore, the estimated values on dq-axis mutual inductance are called cross-coupling factors. The cross-coupling factors are estimated in the process of position estimation. The estimated values are reflected in the controller in the same sampling time as the current control. This method does not require previous analyses such as FEA. This method is expected to decrease position estimation error and increase the robustness of the disturbance. Experimental results express the validity of the proposed method.

This paper is organized as follows: In section II, position and cross-coupling factors estimation method with high frequency voltage injection is explained. In section III, the proposed controller is shown. In section IV, the experimental results are shown. In section V, discussions on the experimental results are described. In section VI, this paper is concluded.

II. POSITION AND CROSS-COUPLING FACTORS ESTIMATION METHOD

This section describes the estimation method of position and dq-axis mutual inductance. This section also reveals that the estimated values of dq-axis mutual inductance in discrete-time systems are part of the actual values. The method is based on d-axis high-frequency voltage injection with square-wave-type voltage synchronized carrier frequency. The electrical coordinate of IPMSM and analysis results of dq-axis inductance are shown in Fig. 2.

A. ESTIMATION ALGORITHM

The α - β frame is fixed to the stator winding. The α -axis coincides with the U-phase. The d-q frame expresses the synchronous reference frame rotated from the α - β frame by

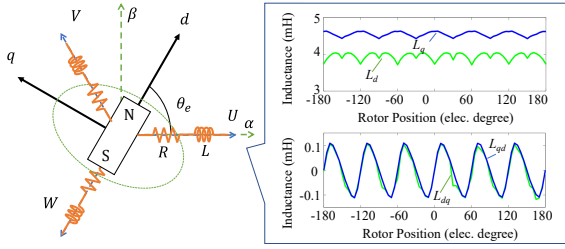


FIGURE 2. Coordinate of IPMSM and dq-axis inductance.

electrical angle θ_e . The d-axis coincides with the N-pole. Variables in this paper are shown in TABLE 1.

The voltage equation in the synchronous reference frame of IPMSMs considering dq-axis mutual inductance is expressed as (1). Though the actual resistance values and inductance values are variable during the operation according to the rotor position, load current, and temperature, they are calculated as static values in the estimation algorithm.

$$\begin{bmatrix} v_d \\ v_q \end{bmatrix} = \begin{bmatrix} R & -\omega_e L_q \\ \omega_e L_d & R \end{bmatrix} \begin{bmatrix} i_d \\ i_q \end{bmatrix} + \begin{bmatrix} L_d & L_{dq} \\ L_{qd} & L_q \end{bmatrix} \frac{d}{dt} \begin{bmatrix} i_d \\ i_q \end{bmatrix} + \begin{bmatrix} 0 \\ \omega_e \Phi \end{bmatrix} \quad (1)$$

The injected voltage and current frequency are set as much higher than the synchronous frequency of the motor. In that case, product terms of inductance and differentiated current are much more significant than the other terms in (1). The voltage equation for the high-frequency component can be approximated as (2). \mathbf{L}_h is a matrix of inductance.

$$\begin{bmatrix} v_{dh} \\ v_{qh} \end{bmatrix} = \begin{bmatrix} L_{dh} & L_{dqh} \\ L_{qdh} & L_{qh} \end{bmatrix} \frac{d}{dt} \begin{bmatrix} i_{dh} \\ i_{qh} \end{bmatrix} = \mathbf{L}_h \frac{d}{dt} \begin{bmatrix} i_{dh} \\ i_{qh} \end{bmatrix} \quad (2)$$

The relationship between α - β frame and d-q frame is expressed as (3).

$$\begin{bmatrix} i_\alpha \\ i_\beta \end{bmatrix} = \begin{bmatrix} \cos \theta_e & -\sin \theta_e \\ \sin \theta_e & \cos \theta_e \end{bmatrix} \begin{bmatrix} i_d \\ i_q \end{bmatrix} \quad (3)$$

This paper focuses on a low-speed operation. Simulation results to compare with the time differential terms of dq-axis current and the velocity terms in the time differential terms of α - β -axis current are shown in Fig. 3. The time differential terms of dq-axis current were large enough to ignore that of the velocity terms. The time differential terms of (3) can be shown as (4).

$$\frac{d}{dt} \begin{bmatrix} i_\alpha \\ i_\beta \end{bmatrix} = \begin{bmatrix} \cos \theta_e & -\sin \theta_e \\ \sin \theta_e & \cos \theta_e \end{bmatrix} \frac{d}{dt} \begin{bmatrix} i_d \\ i_q \end{bmatrix} \quad (4)$$

By combining (2) and (4), high frequency component of current in α - β frame is derived as (5).

$$\frac{d}{dt} \begin{bmatrix} i_{\alpha h} \\ i_{\beta h} \end{bmatrix} = \begin{bmatrix} \cos \theta_e & -\sin \theta_e \\ \sin \theta_e & \cos \theta_e \end{bmatrix} \mathbf{L}_h^{-1} \begin{bmatrix} v_{dh} \\ v_{qh} \end{bmatrix} \quad (5)$$

When the injected voltage is a square wave, the high-frequency voltage can be expressed by (6) in discrete time.

TABLE 1. Symbols and Meaning of Variables in This Paper.

Symbol	Meaning	Symbol	Meaning
v	Voltage	O_d	d-axis component
i, I	Current	O_q	q-axis component
R	Resistance	O_{dq}	Mutual component
L	Inductance	O_{qd}	Mutual component
θ_e	Electrical angle	O^{cmd}	Command
ω_e	Angular velocity	O^{res}	Response
Φ	Linkage magnetic flux	O^{vob}	VDOB
t	Time	O^{dis}	Disturbance
t_s	Sampling time	O^{ff}	Decoupling control
s	Laplace operator	O_h	High-frequency
k, m	Timing of sampling	O_{inj}	Injected value
a, b, c, l	Replacement variable	O_n	Nominal parameter
e	Error	\hat{O}	Estimated value
f	Function for SMC	O_u	U-phase component
K, p, g	Gain	O_v	V-phase component
\mathbf{A}, \mathbf{B}	Arbitrary matrix	O_w	W-phase component
ω_{smc}	Natural frequency	\mathbf{V}	Lyapunov function
ζ_{smc}	Attenuation coefficient	\mathbf{S}	Sliding surface

The d-axis on which the high-frequency voltage is injected does not coincide with the actual d-axis in position-sensorless servo drive systems because of the estimation error. However, the estimation error is assumed to be small enough, and the q-axis part is set to zero.

$$\begin{bmatrix} v_{dh}[k] \\ v_{qh}[k] \end{bmatrix} = \begin{bmatrix} v_h[k] \\ 0 \end{bmatrix} \quad (6)$$

$$v_h[k] = \begin{cases} V_{inj} & (k = 2m) \\ -V_{inj} & (k = 2m + 1) \end{cases}$$

The high-frequency current is expressed as (7).

$$\begin{aligned} \frac{d}{dt} \begin{bmatrix} i_{\alpha h} \\ i_{\beta h} \end{bmatrix} &= \frac{\pm V_{inj}}{L_d L_q - L_{dq} L_{qd}} \begin{bmatrix} L_{qh} \cos \theta_e + L_{qd} \sin \theta_e \\ L_{qh} \sin \theta_e - L_{qd} \cos \theta_e \end{bmatrix} \\ &= a \begin{bmatrix} L_{qh} & L_{qd} \\ -L_{qd} & L_{qh} \end{bmatrix} \begin{bmatrix} \cos \theta_e \\ \sin \theta_e \end{bmatrix} \end{aligned} \quad (7)$$

From (7), the inductance and the position are expressed as (8) and (9), respectively.

$$\begin{bmatrix} L_{qh} \\ L_{qd} \end{bmatrix} = \frac{1}{a} \begin{bmatrix} \cos \theta_e & \sin \theta_e \\ \sin \theta_e & -\cos \theta_e \end{bmatrix} \frac{d}{dt} \begin{bmatrix} i_{\alpha h} \\ i_{\beta h} \end{bmatrix} \quad (8)$$

$$\begin{aligned} \begin{bmatrix} \cos \theta_e \\ \sin \theta_e \end{bmatrix} &= \frac{1}{a (L_{qh}^2 + L_{qd}^2)} \begin{bmatrix} L_{qh} & -L_{qd} \\ L_{qd} & L_{qh} \end{bmatrix} \frac{d}{dt} \begin{bmatrix} i_{\alpha h} \\ i_{\beta h} \end{bmatrix} \\ &= b \begin{bmatrix} 1 & -\frac{L_{qd}}{L_{qh}} \\ \frac{L_{qd}}{L_{qh}} & 1 \end{bmatrix} \frac{d}{dt} \begin{bmatrix} i_{\alpha h} \\ i_{\beta h} \end{bmatrix} \end{aligned} \quad (9)$$

A variable c is defined as (10).

$$c = \frac{L_{qd}}{L_{qh}} = \frac{\frac{di_{\alpha h}}{dt} \sin \theta_e - \frac{di_{\beta h}}{dt} \cos \theta_e}{\frac{di_{\alpha h}}{dt} \cos \theta_e + \frac{di_{\beta h}}{dt} \sin \theta_e} \quad (10)$$

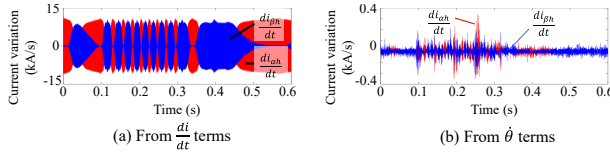


FIGURE 3. Factors in time differential terms of $\alpha\beta$ -axis current.

The position can be estimated as (11) from (9) and (10) by using the addition theorem for inverse trigonometric functions.

$$\hat{\theta}_e = \tan^{-1} \left(\frac{\frac{di_{\beta h}}{dt}}{\frac{di_{\alpha h}}{dt}} \right) + \tan^{-1}(c) \quad (11)$$

The variable c includes L_{qdh} . According to Fig. 2, L_{qdh} and L_{dqh} are approximately same. The nominal value or the actual value of L_{qh} can be obtained from catalogs, nameplates, or measurements. The high-frequency component of dq-axis mutual inductance can be estimated as (12).

$$\hat{L}_{qdh} = \hat{L}_{dqh} = cL_{qn} \quad (12)$$

B. ESTIMATION PROCESSING IN CONTROLLER

In position-sensorless servo drive systems, the algorithm described above is implemented as a discrete-time system. The time differential terms of current can be approximately expressed by (13). Δ denotes first-order backward finite-difference.

$$\frac{d}{dt} \begin{bmatrix} i_{\alpha h} \\ i_{\beta h} \end{bmatrix} = \begin{bmatrix} \Delta i_{\alpha}[k] \\ \Delta i_{\beta}[k] \end{bmatrix} = \frac{1}{t_s} \begin{bmatrix} i_{\alpha}[k] - i_{\alpha}[k-1] \\ i_{\beta}[k] - i_{\beta}[k-1] \end{bmatrix} \quad (13)$$

Equations (8) and (9) are rewritten as (14) and (15), respectively.

$$\begin{bmatrix} L_{qh}[k] \\ L_{qdh}[k] \end{bmatrix} = \frac{1}{a} \begin{bmatrix} \cos \theta_e[k] & \sin \theta_e[k] \\ \sin \theta_e[k] & -\cos \theta_e[k] \end{bmatrix} \begin{bmatrix} \Delta i_{\alpha}[k] \\ \Delta i_{\beta}[k] \end{bmatrix} \quad (14)$$

$$\begin{bmatrix} \cos \theta_e[k] \\ \sin \theta_e[k] \end{bmatrix} = b \begin{bmatrix} 1 & -\frac{L_{qdh}[k]}{L_{qh}[k]} \\ \frac{L_{qdh}[k]}{L_{qh}[k]} & 1 \end{bmatrix} \begin{bmatrix} \Delta i_{\alpha}[k] \\ \Delta i_{\beta}[k] \end{bmatrix} \quad (15)$$

In order to derive $c[k]$, $\theta_e[k]$ is required. However, $\theta_e[k]$ still have not been estimated in this cycle calculation in discrete-time systems. The difference between the actual position and the last estimated position is assumed to be negligible since the sampling time is short enough. The assumption shown as (16) is used until $\hat{\theta}_e[k]$ is derived.

$$\theta_e[k] \approx \hat{\theta}_e[k-1] \quad (16)$$

By using this assumption, $c[k]$ is derived as (17).

$$c[k] = \frac{\Delta i_{\alpha}[k] \sin \hat{\theta}_e[k-1] - \Delta i_{\beta}[k] \cos \hat{\theta}_e[k-1]}{\Delta i_{\alpha}[k] \cos \hat{\theta}_e[k-1] + \Delta i_{\beta}[k] \sin \hat{\theta}_e[k-1]} \quad (17)$$

The position at sampling timing k can be estimated as (18).

$$\hat{\theta}_e[k] = \tan^{-1} \left(\frac{\Delta i_{\beta}[k]}{\Delta i_{\alpha}[k]} \right) + \tan^{-1}(c[k]) \quad (18)$$

The estimation of (18) is from some assumptions. The errors from these assumptions decrease the accuracy of the estimated value. Then, in order to decrease the effect, a gain g ($0 \leq g \leq 1$) can be applied. (18) can be rewritten as (19).

$$\hat{\theta}_e[k] = \tan^{-1} \left(\frac{\Delta i_{\beta}[k]}{\Delta i_{\alpha}[k]} \right) + g \tan^{-1}(c[k]) \quad (19)$$

From (17), $\tan^{-1}(c[k])$ can be expressed as (20).

$$\tan^{-1}(c[k]) = \theta_e[k-1] - \tan^{-1} \left(\frac{\Delta i_{\beta}[k]}{\Delta i_{\alpha}[k]} \right) \quad (20)$$

Therefore, (21) is derived by (19) and (20).

$$\hat{\theta}_e[k] = (1-g) \tan^{-1} \left(\frac{\Delta i_{\beta}[k]}{\Delta i_{\alpha}[k]} \right) + g \hat{\theta}_e[k-1] \quad (21)$$

Equation (21) shows that the estimation method works as a first-order low-pass filter (LPF). If g is zero, the estimated position is the same as that from the voltage equation without considering the dq-axis mutual inductance. From (20) and (21), $c[k]$ can be expressed as (22).

$$\begin{aligned} \tan^{-1}(c[k]) &= g \tan^{-1}(c[k-1]) + \tan^{-1} \left(-\frac{\Delta i_{\beta}[k]}{\Delta i_{\alpha}[k]} \right) \\ &\quad - \tan^{-1} \left(-\frac{\Delta i_{\beta}[k-1]}{\Delta i_{\alpha}[k-1]} \right) \end{aligned} \quad (22)$$

Equation (22) shows that $c[k]$ is derived through a first-order high-pass filter (HPF). The high-frequency component of dq-axis mutual inductance in each sampling timing k can be estimated by (23) as with (12).

$$\hat{L}_{qdh}[k] = \hat{L}_{dqh}[k] = c[k]L_{qn} \quad (23)$$

The equations (20), (21), and (23) mean that the detected current is transformed to position information as the low-frequency component and inductance information as the high-frequency component. The difference between conventional methods with reference tables and the proposed method is shown in Fig. 4. Conventional methods with reference tables use the estimated position to reference the inductance table. Therefore, the fluctuation bandwidth of derived L_{qd} and L_{dq} are in the same bandwidth as the estimated position. On the other hand, the bandwidth of \hat{L}_{qdh} and \hat{L}_{dqh} using (17) by the proposed method are between the cut-off frequency by g and injected voltage frequency. Therefore, the estimated values of dq-axis mutual inductance are part of the actual inductance values, and they are called cross-coupling factors in this paper.

III. PROPOSED CURRENT CONTROL

In this section, the proposed current control method is explained. The current control method is comprised of a sliding-mode controller (SMC) and voltage disturbance observer (VDOB). The current controller is based on the voltage equation considering dq-axis mutual inductance. Since

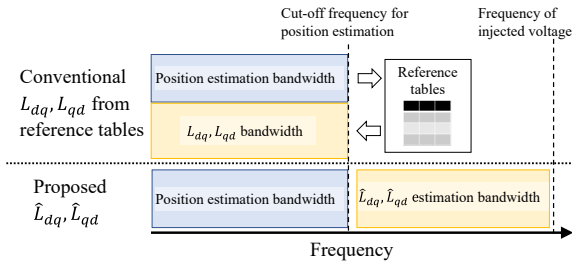


FIGURE 4. The difference between conventional methods and the proposed method in the view of frequency bandwidth.

the actual values of dq-axis mutual inductance cannot be obtained, the estimated cross-coupling factors are utilized online.

The state-space representation of the voltage equation on IPMSM resistance and inductance for the proposed controller is expressed as (24). The speed electromotive force terms and the parameters fluctuation of R , L_d , and L_q are considered as disturbances and included in D .

$$\frac{d}{dt}i = Ai + Bv + D \quad (24)$$

Each element is expressed by equations from (25) to (29).

$$i = \left[\int i_d dt \quad i_d \quad \int i_q dt \quad i_q \right]^T \quad (25)$$

$$v = \begin{bmatrix} v_d & v_q \end{bmatrix}^T \quad (26)$$

$$l = L_{dn}L_{qn} - \hat{L}_{dqh}\hat{L}_{qdh} \quad (27)$$

$$A = \begin{bmatrix} 0 & 1 & 0 & 0 \\ 0 & -\frac{L_{qn}R_n}{l} & 0 & \frac{\hat{L}_{dqh}R_n}{l} \\ 0 & 0 & 0 & 1 \\ 0 & \frac{\hat{L}_{qdh}R_n}{l} & 0 & -\frac{L_{dn}R_n}{l} \end{bmatrix} \quad (28)$$

$$B = \begin{bmatrix} 0 & \frac{L_{qn}}{l} & 0 & -\frac{\hat{L}_{qdh}}{l} \\ 0 & -\frac{\hat{L}_{dqh}}{l} & 0 & \frac{L_{dn}}{l} \end{bmatrix}^T \quad (29)$$

As shown in Fig. 2, the denominator $L_{dn}L_{qn} - \hat{L}_{dqh}\hat{L}_{qdh}$ cannot be zero since self-inductance values are higher than mutual inductance values. The current error between the command and the response is defined as (30).

$$e = i^{res} - i^{cmd} \quad (30)$$

The proposed sliding mode controller is expressed as (31).

$$v^{cmd} = -(p^T B)^{-1} p^T A e - (p^T B)^{-1} K f(p^T e) \quad (31)$$

The gains p and K is defined by (32) and (33), respectively.

$$p = \begin{bmatrix} p_d & p_q \end{bmatrix} = \begin{bmatrix} p_{d1} & p_{d2} & p_{d3} & p_{d4} \\ p_{q1} & p_{q2} & p_{q3} & p_{q4} \end{bmatrix}^T \quad (32)$$

$$K = \begin{bmatrix} K_d & 0 \\ 0 & K_q \end{bmatrix} \quad (33)$$

The f is a saturation function expressed by (34) and (35) to avoid the chattering from signature function.

$$f(p^T e) = \begin{bmatrix} \text{sat}_u(p_d^T e) & \text{sat}_u(p_q^T e) \end{bmatrix}^T \quad (34)$$

$$\text{sat}_u(x) = \begin{cases} 1 & (x > 1) \\ x & (-1 \leq x \leq 1) \\ -1 & (x < -1) \end{cases} \quad (35)$$

In the sliding surface S , (36) can be expressed. The integral terms are transformed to Laplace operator s .

$$\begin{aligned} S &= p^T e \\ &= ((p_{d3}p_{q1} - p_{d1}p_{q3}) + (p_{d4}p_{q2} - p_{d2}p_{q4})s^2 \\ &\quad + (p_{d3}p_{q2} + p_{d4}p_{q1} - p_{d2}p_{q3} - p_{d1}p_{q4})s) \begin{bmatrix} e_d \\ e_q \end{bmatrix} \\ &= 0 \end{aligned} \quad (36)$$

The natural frequency ω_{smc} and the attenuation coefficient ζ_{smc} can be written as (37) and (38).

$$\omega_{smc} = \sqrt{\frac{p_{d3}p_{q1} - p_{d1}p_{q3}}{p_{d4}p_{q2} - p_{d2}p_{q4}}} \quad (37)$$

$$\zeta_{smc} = \frac{p_{d3}p_{q2} + p_{d4}p_{q1} - p_{d2}p_{q3} - p_{d1}p_{q4}}{2\omega_{smc}(p_{d4}p_{q2} - p_{d2}p_{q4})} \quad (38)$$

Gains in p can be designed to set desired ω_{smc} and ζ_{smc} .

When Lyapunov function V is defined, the time differential term of V is expressed as (39).

$$\begin{aligned} \frac{d}{dt}V &= \frac{d}{dt} \left(\frac{1}{2} S^T S \right) \\ &= S^T (p^T D - K f(S)) \end{aligned} \quad (39)$$

The sliding mode exists when K_d and K_q are enough larger than disturbances.

VDOB modifies the voltage command calculated by SMC. The block diagram of current control is shown in Fig. 5. Since the model-based resistance compensation is applied to each UVW-phase after VDOB, VDOB includes only inductance.

By using VDOB, the disturbances D including parameter variations are compensated in the bandwidth of the cut-off frequency. Therefore, although inductance values vary with the rotor position, as shown in Fig. 2, the parameters can be assumed to be constant at the nominal values in the low-speed range. In other bandwidth, SMC compensates for uncertainties of the system. Generally, K_d and K_q are required to be high enough to suppress the disturbance. As the proposed controller uses SMC and VDOB considering cross-coupling factors, K_d and K_q can be set as practical values independently of noise effects.

Furthermore, in this research, the PI current controller considering cross-coupling factors compensation in the decoupling control is utilized to compare with the performance of the proposed controller. The output of decoupling control

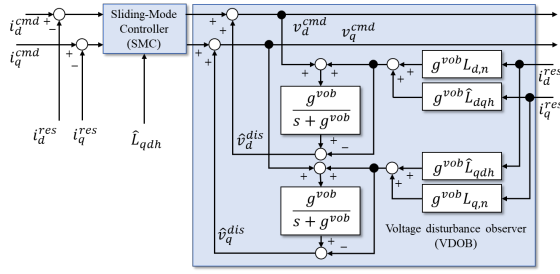


FIGURE 5. Block diagram of proposed current control.

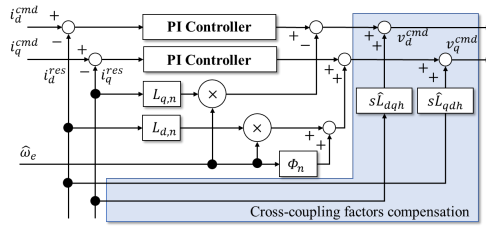


FIGURE 6. Block diagram of a compared controller with a conventional PI controller with cross-coupling factors compensation.

is expressed as (40) from (1). A phase-lock-loop (PLL) derives $\hat{\omega}_e$ after position estimation processing.

$$\begin{bmatrix} v_d^{ff} \\ v_q^{ff} \end{bmatrix} = \begin{bmatrix} 0 & -\hat{\omega}_e L_{qn} \\ \hat{\omega}_e L_{dn} & 0 \end{bmatrix} \begin{bmatrix} i_d^{res} \\ i_q^{res} \end{bmatrix} + \begin{bmatrix} 0 \\ \hat{\omega}_e \Phi_n \end{bmatrix} + \begin{bmatrix} s \hat{L}_{dqh} i_q^{res} \\ s \hat{L}_{qdh} i_d^{res} \end{bmatrix} \quad (40)$$

The block diagram of the PI current controller considering cross-coupling factors is shown as Fig. 6.

IV. EXPERIMENTAL RESULTS

A. SETUP

In this section, experimental results are shown. The responses from four control systems in TABLE 2 were compared. The experiments were on the estimation error, position control response, and torque-velocity characteristics. The electric and mechanical angles units are expressed differently as “elec.” and “mech.” respectively.

The experimental setup is shown in Fig. 7. The motors were SGM7A-04AFA61 and SGM7J-04A7A61. SGM7J-04A7A61 was the test motor, and SGM7A-04AFA61 was the load motor. Their shafts were connected by a coupling. Though each motor had encoders, the information was only for the actual response confirmation. The motion controller and the oscilloscope recorded the experimental data. They were made by YASKAWA Electric Corporation.

The block diagrams for the experiments are shown in Fig. 8 and Fig. 9. Fig. 8 was for “PI I” and “PI II.” Fig. 9 was for “SMC I” and “SMC II”. The blue part was implemented on the motion controller, and the yellow part was implemented on the functional test board. The motion controller had a P-PI type position controller and a LPF for torque

TABLE 2. Main Different Points of Confirmed Four Control Methods.

Methods Name	Controller	g (Cut-off frequency)	i_d^{cmd}
PI I	PI controller	0.8 (424 Hz)	1 %
PI II	PI controller	0.8 (424 Hz)	5 %
SMC I	SMC	0	1 %
SMC II (Proposed)	SMC	0.5 (1698 Hz)	1 %

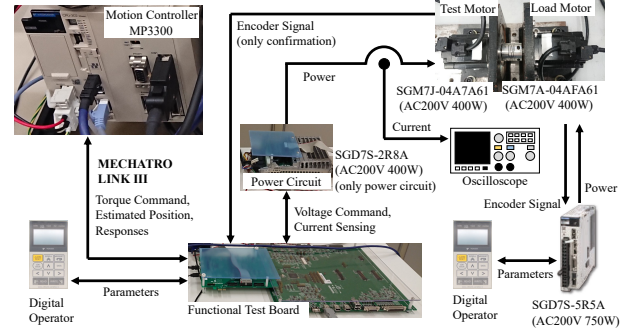


FIGURE 7. Experimental setup.

command. Although the control methods are expressed as continuous-time systems in section III, they were implemented on the controller as discrete-time systems. Laplace operator s was approximated by a first-order backward difference to save the memory and reduce processing time.

The differential methods for rotor velocity were different according to the control methods. The velocity response was derived by a first-order backward difference of the estimated position in the motion controller of Fig. 8. The estimated velocity response is derived by a PI type phase-lock-loop (PLL) in Fig. 8. Since the responses by the controller shown in Fig. 9 had smaller vibrations, the LPF function in (21) was enough to estimate position. However, the first-order backward difference amplifies the vibration. Therefore, the estimated velocity response was derived by pseudo differentiation in Fig. 9. Since the estimated velocity response was used only in the motion controller, the calculation of pseudo differentiation was implemented on the motion controller.

Control parameters including sampling periods are shown in TABLE 3 and (41).

$$\mathbf{p} = \begin{bmatrix} 1333 & 1.4 & 27 & 0.0025 \\ 27 & 0.0025 & 1333 & 1.8 \end{bmatrix}^T \quad (41)$$

The test motor parameters are shown in TABLE 4. Parameters shown in TABLE 3 were adjusted by trial and error to prevent significant vibration in a steady state. The sampling period of current control was decided from the carrier frequency 10.7 kHz. The sampling periods of the motion control were adjusted to reduce vibration while checking the response. Gains in \mathbf{p} were adjusted to make ω_{smc} and ζ_{smc} 133 Hz and 1, respectively. Gains K_d and K_q were decided by trial and error. The PI controller frequency characteristic and VDOB cut-off frequencies were adjusted to be similar, and the values were larger than the electrical velocity in the low-speed range, which was under 20 % rated

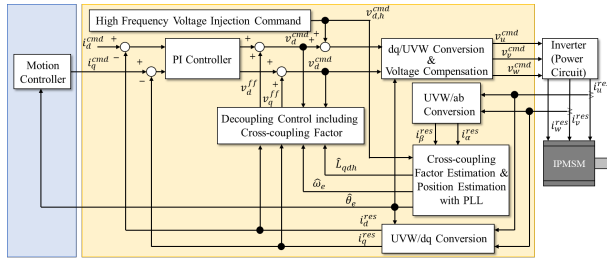


FIGURE 8. Block diagram of the control method with PI controller.

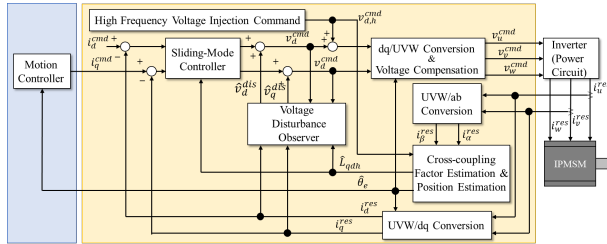


FIGURE 9. Block diagram of the control method with SMC.

speed (314 elec. rad/s). Though the motion control gains and sampling time of “PI I” and “PI II” were lower than those of “SMC I” and “SMC II,” these parameters adjustment was based on the same policy to prevent significant vibration.

B. RESULTS ON POSITION ESTIMATION ERROR

In this experiment, the error between the estimated position and the detected position by the encoder was compared. The electric angle was shifted by 4 degrees and by 30 degrees, and position control was performed for 0.6 s at each angle. In each angle, estimated position and actual position obtained by the encoder was sampled. The sampling time was 1 ms. The compared methods are “SMC I” and “SMC II” to reveal the difference from the considering dq-axis mutual inductance. The average estimation error is shown in Fig. 10. The variance of estimation error is shown in Fig. 11. The red points are “SMC I” results, and the blue points are “SMC II” results. As Fig. 10 and Fig. 11 show, the maximum average value of “SMC II” was larger than that of “SMC I.” On the other hand, the maximum variance value of “SMC II” was smaller than that of “SMC I.” When the estimation error variance was large, the estimated position had a vibration. The fast Fourier transform (FFT) results of the estimated position at 60 elec. degree and 108 elec. degree are shown in Fig. 12 as examples. As Fig. 12 and Fig. 13 show, the peak level of “SMC II” was smaller than that of “SMC I.”

C. RESULTS OF POSITION CONTROL RESPONSE

In this experiment, the command tracking performance and the vibration during position control were verified. The position command was increased in constant until the target position was 25.1 mech. rad. The increased value was equivalent to 3.14 mech. rad/s, which is 1 % of the rated speed. The compared methods were “PI I,” “SMC I,” and “SMC II” to reveal the difference of the response and vibration during the control methods and estimation methods. The experimental results are shown in Fig. 14, Fig. 15, Fig. 16, and Fig. 17.

TABLE 3. Control Parameters for Experiments.

Parameter	“PI I”	“PI II”	“SMC I”	“SMC II”
Sampling Period (Motion) (μ s)	2000			125
Sampling Period (Current) (μ s)	94			94
Position Proportional Gain (1/s)	2			32
Velocity Proportional Gain (rad/s)	32			94
Velocity Integral Gain (s)	0.02			0.003
Cut-off frequency of Torque Filter (rad/s)	250			250
Cut-off frequency of Pseudo differentiation (rad/s)	-			1600
Gain in Position Estimation	0.8		0.0	0.5
d-axis Proportional Gain (rad/s)	1005		-	-
d-axis Integral Gain (ms)	1.3		-	-
q-axis Proportional Gain (rad/s)	1005		-	-
q-axis Integral Gain (ms)	1.6		-	-
SMC Gains K_d, K_q	-			21
VDOB gain g^{vob} (rad/s)	-			1099
PLL Cut-off frequency (rad/s)	144		-	-

TABLE 4. Nominal Parameters of The Test Motor.

Parameter	Value
R (Ohm)	1.4
L_d (mH)	1.9
L_q (mH)	2.3
Torque constant (Nm/A)	0.544
Φ (V/(elec. rad/s))	0.109
Rotor inertia (kgm^2)	0.486×10^{-4}
Viscosity friction coefficient (Nm/(rad/s) (Mechanical))	6.8×10^{-5}
Rated Power (W)	400
Rated velocity (mech. rad/s)	314.2
Rated torque (Nm)	1.27
Pole pairs	5

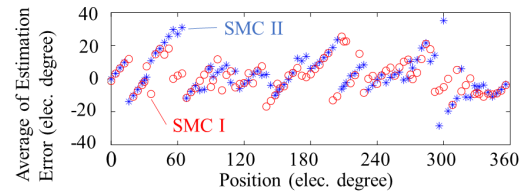


FIGURE 10. Average of position estimation error.

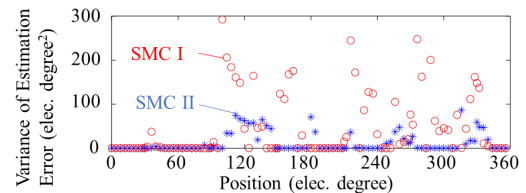


FIGURE 11. Variance of position estimation error.

lent to 3.14 mech. rad/s, which is 1 % of the rated speed. The compared methods were “PI I,” “SMC I,” and “SMC II” to reveal the difference of the response and vibration during the control methods and estimation methods. The experimental results are shown in Fig. 14, Fig. 15, Fig. 16, and Fig. 17.

Fig. 14 shows the position command and position responses. All position responses have followed the command and achieved the target position.

Fig. 15 shows the velocity responses with a 2.5 Hz LPF

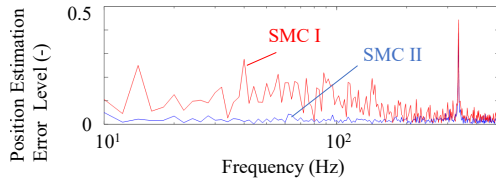


FIGURE 12. FFT results of estimated position at 60 elec. degree.

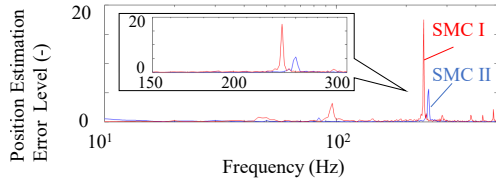


FIGURE 13. FFT results of estimated position at 108 elec. degree.

applied. According to Fig. 15, the velocity responses of “SMC I” and “SMC II” quickly rose. The responses of “SMC I” and “SMC II” were almost the same. However, the rising time of “PI I” was longer than those of “SMC I” and “SMC II” as the “PI I” had lower motion control gains. The peaks of vibration in steady-state velocity between 2.5 s and 8 s were similar for the three methods.

The difference in the vibration can be confirmed in Fig. 16 and Fig. 17. These figures show the FFT results of the velocity response and the current response from 0.5 s to 2.5 s (2000 sampling points). In Fig. 16, “PI I” had a higher level than “SMC I” and “SMC II” over 10 Hz, which was over the control bandwidth of “PI I,” although “PI I” had slower responses. The FFT results of “SMC I” and “SMC II” were similar under the velocity control bandwidth. In addition, the peak levels of “SMC I” and “SMC II” were smaller than that of “PI I.” Therefore, velocity control performance can be improved by sliding mode current control. However, the level of “SMC I” was larger than that of “SMC II” around 220 Hz, which was over the current control bandwidth. A similar difference over the current control bandwidth can be shown in Fig. 17. “SMC II” had the estimated cross-coupling factors in the controller. Therefore, current control performance can be improved by using estimated cross-coupling factors.

D. TORQUE-VELOCITY CHARACTERISTICS

In this experiment, it was confirmed for how much load torque the system could operate without stalling for each velocity command. The load torque that was applied by the load motor was gradually increased for each velocity command. The velocity commands were shifted by 6.28 mech. rad/s up to 62.8 mech. rad/s, which was 20 % of the rated speed. The operation in each velocity command was stopped when the load motor rotated the test motor, or the error between the estimated position and the detected position was larger than 1 rad. The load torque values, which were at the stop timing, were measured. The measured values are shown in

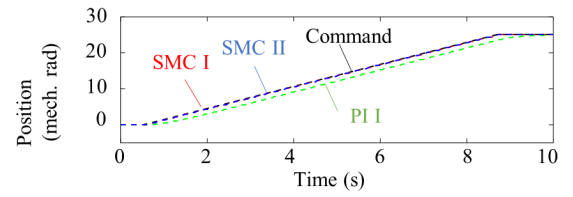


FIGURE 14. Position response.

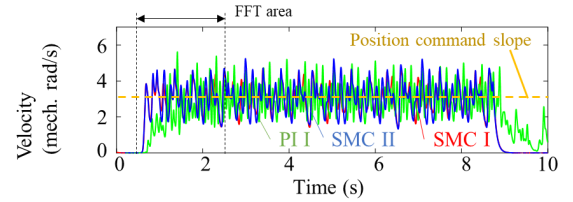


FIGURE 15. Velocity response in time domain.

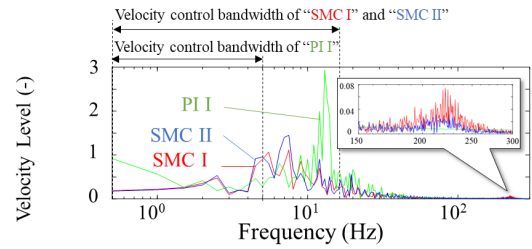


FIGURE 16. FFT results of velocity response.

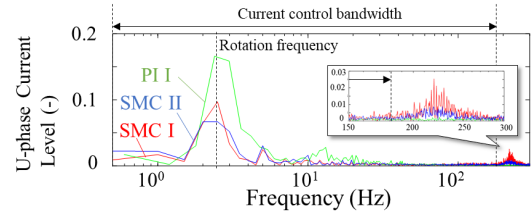


FIGURE 17. FFT results of current response.

Fig. 18. According to Fig. 18, the test motor could operate from low-speed range to high load torque of nearly 100 % of rated torque with “SMC II.”

In “PI I,” the test motor did not start properly with the load motor. In “PI II,” the test motor was out of control in low-speed under 31 mech. rad/s (10 % of rated speed) with 0.2 Nm (15 % of rated torque), and it was out of control at 63 mech. rad/s (20 % of rated torque). However, it was possible to operate under a load torque of more than 1 Nm (90 % of rated torque).

In “SMC I” and “SMC II,” similar characteristics were confirmed. “SMC II” was more robust than “SMC I.” It was able to operate more than 15 mech. rad/s under an external

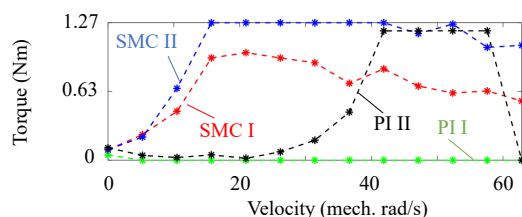


FIGURE 18. Torque-velocity characteristics.

torque of more than 1 Nm.

V. DISCUSSION

In this section, discussions of the experimental results are described. “SMC II” had large average estimated errors around 60 elec. degree and 300 elec. degree but smaller variance over a wide range of electrical angles in Fig. 10 and Fig. 11. The maximum value of the variance was less than one-third. Since the variance in “SMC I” exceeded 100 elec. degree², the instantaneous estimation error can be more than 10 elec. degree higher than the average values. As shown in Fig. 12 and Fig. 13, the frequency of position estimation vibration was over 10 Hz, which was higher than the motion control bandwidth. The peak frequency was around 220 Hz, which was higher than the current control bandwidth. The vibration was a disturbance for the controller, and the sensitivity function effect cannot be ignored. Therefore, less variance in the estimated positions over a wide range of electrical angles is desired to allow a more stable operation. The estimated positions in “SMC II” had smaller estimation error variances and vibration by applying the dq-axis mutual inductance model in the estimation algorithm. In addition, “SMC II” had the LPF function, as shown in (21). As TABLE 2 shows, the cut-off frequency was 1698 Hz, which was much higher than that of generally used PLL. Therefore, the estimated positions in “SMC II” are more reliable than the conventional estimated position because there is small variability and phase delay from the filter.

According to Fig. 16 and Fig. 17, the levels were large around 220 Hz. Since the cut-off frequency of VDOB was 1099 rad/s (175 Hz), it was related to the sensitivity function of VDOB. When the controller had no model on dq-axis mutual inductance, the mutual interferences from the other axis were all disturbance for the controller. In “SMC II”, SMC and VDOB had the cross-coupling factors, and the mutual interferences were compensated in the controller. On the other hand, “SMC I” did not have the cross-coupling factors and the mutual interferences were disturbance, and the vibration occurred.

The higher robustness of “SMC II” shown in Fig. 18 came from the above two advantages. Although the effect of the absolute error of the estimated value remains, the robustness to the actual mechanical external force has been improved because it is not necessary to compensate for the variance of the estimated position and the mutual interference of the

current during rotation as disturbances. All experimental results show the control performance of “PI I” and “PI II” were worse than that of “SMC I” and “SMC II.” The integral gain cannot be high because of uncertainty in the PI controller. Low-gain PI controllers cannot adequately compensate for the effects of estimation error and model uncertainty. By using SMC, the uncertainty is compensated by the robustness of the controller. Therefore, the current controller with SMC and VDOB considering cross-coupling factors is suitable for position-sensorless servo drive systems.

The theory of the proposed method is based on many assumptions. It is easily considered that these assumptions may not be valid during operation. However, as the experimental results show the effectiveness, considering dq-axis mutual inductance in position-sensorless control is significant. In future work, the estimation method without the above assumptions will be proposed to realize higher robustness and reliable position estimation.

VI. CONCLUSIONS

This paper presented SMC with cross-coupling factors estimation for position-sensorless servo drive systems. The controller also included VDOB. The cross-coupling factors from dq-axis mutual inductance were estimated in the process of position estimation with high-frequency voltage injection and reflected the current controller in each sampling time. The proposed control method realized a smaller variance of estimated position, smaller vibration, and better velocity-torque characteristics according to experimental results. The estimation method without the assumptions for discrete-time processing will be proposed in future work.

REFERENCES

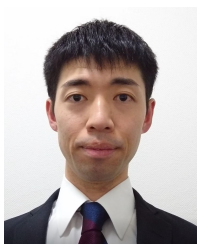
- [1] S.-K. Sul, Y.-C. Kwon, and Y. Lee, “Sensorless control of IPMSM for last 10 years and next 5 years,” *CES Trans. on Elect. Mach. and Syst.*, vol. 1, no. 2, pp. 91–99, 2017.
- [2] G. Wang, M. Valla, and J. Solsona, “Position Sensorless Permanent Magnet Synchronous Machine Drives-A Review,” *IEEE Trans. Ind. Electron.*, vol. 67, no. 7, pp. 5830–5842, 2020.
- [3] J. M. Liu and Z. Q. Zhu, “Improved Sensorless Control of Permanent-Magnet Synchronous Machine Based on Third-Harmonic Back EMF,” *IEEE Trans. Ind. Appl.*, vol. 50, no. 3, pp. 1861–1870, 2014.
- [4] J. Kim, I. Jeong, K. Nam, J. Yang and T. Hwang, “Sensorless Control of PMSM in a High-Speed Region Considering Iron Loss,” *IEEE Trans. Ind. Electron.*, vol. 62, no. 10, pp. 6151–6159, 2015.
- [5] R. Antonello, L. Ortombina, F. Tinazzi, and M. Zigliotto, “Enhanced Low-Speed Operations for Sensorless Anisotropic PM Synchronous Motor Drives by a Modified Back-EMF Observer,” *IEEE Trans. Ind. Electron.*, vol. 65, no. 4, pp. 3069–3076, 2018.
- [6] J.-I. Ha, K. Ide, T. Sawa, and S.-K. Sul, “Sensorless Position Control and Initial Position Estimation of an Interior Permanent Magnet Motor,” in *Proc. the 2001 IEEE Industry Appl. Conf. 36th IAS Annu. Meeting*, vol. 4, Sept. 2001, pp. 2607–2613.
- [7] J.-H. Im and R.-Y. Kim, “Improved Saliency-Based Position Sensorless Control of Interior Permanent-Magnet Synchronous Machines With Single DC-Link Current Sensor Using Current Prediction Method,” *IEEE Trans. Ind. Electron.*, vol. 65, no. 7, pp. 5335–5343, 2018.
- [8] Z. Zhang, C. Hu, Y. Zhang, and W. Shen, “Research on High Frequency Voltage Injection Method for PMSM,” in *Proc. 2019 14th IEEE Conf. Ind. Electron. Appl.*, June 2019, pp. 266–269.
- [9] R. Ni, K. Lu, F. Blaabjerg, and D. Xu, “A comparative study on pulse sinusoidal high frequency voltage injection and INFORM methods for

- PMSM position sensorless control,” in *Proc IECON 2016 - 42nd Annu. Conf. the IEEE Ind. Electron. Soc.*, Oct. 2016, pp. 2600–2605.
- [10] Y.-D. Yoon, S.-K. Sul, S. Morimoto, and K. Ide, “High-Bandwidth Sensorless Algorithm for AC Machines Based on Square-Wave-Type Voltage Injection,” *IEEE Trans. Ind. Appl.*, vol. 47, no. 3, pp. 1361–1370, 2011.
 - [11] A. Ravilumar Setty, S. Wekhande, and K. Chatterjee, “Compensation of rotor position estimation error due to stator winding resistance in signal injection based sensor less PMSM drives,” in *Proc. 2013 IEEE Int. Symp. Sensorless Control for Elect. Drives and Predictive Control of Elect. Drives and Power Electron.*, Oct. 2013, pp. 1–5.
 - [12] Z. Q. Zhu, Y. Li, D. Howe, and C. M. Bingham, “Compensation for Rotor Position Estimation Error due to Cross-Coupling Magnetic Saturation in Signal Injection Based Sensorless Control of PM Brushless AC Motors,” in *Proc. 2007 IEEE Int. Electric Mach. Drives Conf.*, vol. 1, pp. 208–213, 2007.
 - [13] S. Morimoto, K. Shimamoto, and T. Hanamoto, “Realization of High Torque Density Encoderless Servo Drive System,” in *Proc IECON 2019 - 45th Annu. Conf. the IEEE Ind. Electron. Soc.*, vol. 1, Oct. 2019, pp. 1284–1289.
 - [14] S. Morimoto, K. Shimamoto, M. Kakiyama, and T. Hanamoto, “Improving Position Estimation Accuracy of Magnetic Saliency Based Sensorless Control by Considering Cross-Coupling Factor,” *IEEJ Journal of Ind. Appl.*, vol. 10, no. 1, pp. 18–26, 2021.
 - [15] C. Li, G. Wang, G. Zhang, D. Xu, and D. Xiao, “Saliency-Based Sensorless Control for SynRM Drives With Suppression of Position Estimation Error,” *IEEE Trans. Ind. Electron.*, vol. 66, no. 8, pp. 5839–5849, 2019.
 - [16] L. Chang and T. M. Jahns, “Prediction and Evaluation of PWM-Induced Current Ripple in IPM Machines Incorporating Slotting, Saturation, and Cross-Coupling Effects,” *IEEE Trans. Ind. Appl.*, vol. 54, no. 6, pp. 6015–6026, 2018.
 - [17] K. Shimamoto and S. Morimoto, “Position Estimation Accuracy Improvement for Magnetic Saliency Based Sensorless Control Including Cross-Coupling Factor,” in *Proc 2018 Int. Power Electron. Conf.*, May 2018, pp. 2210–2215.
 - [18] J.-Y. Chen and S.-C. Yang, “Saliency-Based Permanent Magnet Machine Position Sensorless Drive Using Proposed PWM Injection and Shunt-Based Current Sensing for Position Estimation,” *IEEE Trans. Ind. Electron.*, vol. 68, no. 7, pp. 5693–5703, 2021.
 - [19] K. Shimamoto, “Estimation of dq-axis Mutual Inductances for Vibration Reduction of Encoderless Control,” in *Proc 2021 IEEE 30th Int. Symp. Ind. Electron.*, June 2021, pp. 1–6.
 - [20] G.-D. Andreescu, C. Pitic, F. Blaabjerg, and I. Boldea, “Combined Flux Observer With Signal Injection Enhancement for Wide Speed Range Sensorless Direct Torque Control of IPMSM Drives,” *IEEE Trans. Energy Convers.*, vol. 23, no. 2, pp. 393–402, 2008.
 - [21] S. Sayeef, G. Foo, and M. F. Rahman, “Rotor Position and Speed Estimation of a Variable Structure Direct-Torque-Controlled IPM Synchronous Motor Drive at Very Low Speeds Including Standstill,” *IEEE Trans. Ind. Electron.*, vol. 57, no. 11, pp. 3715–3723, 2010.
 - [22] G. Wang, Z. Li, G. Zhang, Y. Yu, and D. Xu, “Quadrature PLL-Based High-Order Sliding-Mode Observer for IPMSM Sensorless Control With Online MTPA Control Strategy,” *IEEE Trans. Energy Convers.*, vol. 28, no. 1, pp. 214–224, 2013.
 - [23] M. X. Bui, M. F. Rahman and D. Xiao, “A Hybrid Sensorless Controller of an Interior Permanent Magnet Synchronous Machine Using Current Derivative Measurements and a Sliding Mode Observer,” *IEEE Trans. Ind. Appl.*, vol. 56, no. 1, pp. 314–324, 2020.



TOSHIYUKI MURAKAMI (M'93 - SM'13) received the B.E., M.E., and Ph.D. degrees in electrical engineering from Keio University, Yokohama, Japan, in 1988, 1990, and 1993, respectively. In 1993, he joined the Department of Electrical Engineering, Keio University, where he is currently a Professor with the Department of System Design Engineering. From 1999 to 2000, he was a Visiting Researcher with the Institute for Power Electronics and Electrical Drives, Aachen University of Technology, Aachen, Germany. His research interests include robotics, intelligent vehicle, mobile robots, and motion control. In the education project, he was a coordinator of the European Master on Advanced Robotics (EMARO), Erasmus Program, from 2008 to 2018. Since 2019, he has been a responsible person of the Japan Europe Master on Advanced Robotics (JEMARO), Erasmus and MEXT Program with the Faculty of Science and Technology, Keio University.

...



KEITA SHIMAMOTO (M'12) received the B.E. degree in system design engineering and the M.E. degree in integrated design engineering from Keio University, Yokohama, Japan, in 2012 and 2014, respectively. He is currently at the Tsukuba Research Laboratory in YASKAWA Electric Corporation and pursuing the Ph.D. degree with the Graduate School of Science and Technology, Keio University. He has worked on research of motion control technology.